Influence of microporosity distribution on the mechanical behavior of oolithic carbonate rocks

J.B. Regnet [a,b], C. David [a,*], J. Fortin [b], P. Robion [a], Y. Makhloufi [c], P.Y. Collin [c]

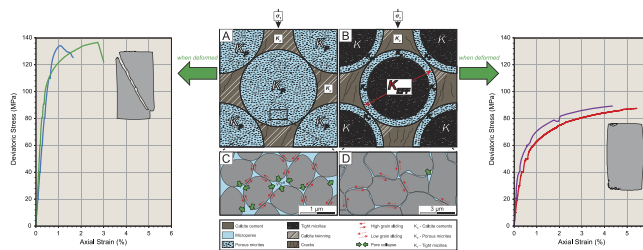[a] Université de Cergy-Pontoise, Laboratoire Géosciences et Environnement Cergy, France
[b] Laboratoire de Géologie de l'Ecole Normale Supérieure, PSL Research University, UMR CNRS 8538, Paris, France
[c] Université de Bourgogne, UMR CNRS 6282 Biogéosciences, Dijon, France

HIGHLIGHTS

- Oolithic carbonate rocks from the Paris Basin are studied under in situ conditions.
- Elastic and mechanical properties are controlled by porosity distribution in micrite.
- Permeability and cap models explain the contrasting behavior with pore distribution.

GRAPHICAL ABSTRACT

ARTICLE INFO

ABSTRACT

The mechanical behavior of oolithic carbonate rocks was investigated for selected rocks with two different microstructural attributes: uniform (UP) and rimmed (RP) distribution of microporosity within ooids. These oolithic carbonate rocks are from the Oolithe Blanche formation, a deep saline aquifer in the Paris Basin, and a possible target for CO_2 sequestration and geothermal production. Samples of similar physical properties (porosity, grain diameter, cement content) but different microporosity textures were deformed under triaxial configuration, in water saturated conditions, at 28 MPa of confining pressure, 5 MPa of pore pressure and at a temperature of 55 °C. During the experiments, acoustic velocities were monitored, and permeability was measured. The results show that the mechanical behavior of these microporous carbonates are strongly controlled by the microporosity distribution within the grains, at the origin of variations in elastic properties, mechanical strength and failure mode. The lower velocities measured in UP samples indicate a larger compliance of the whole structure. The mechanical response indicates that UP samples are characterized by a ductile behavior whereas RP samples display a brittle behavior. Using a conceptual model for the failure envelope of both rocks, our observations can be accounted for if one considers a significant variation of the critical pressure P^*, with UP samples having a lower P^* than RP samples. The permeability evolution under stress was

* Correspondence to: Université de Cergy-Pontoise, Laboratoire Géosciences et Environnement Cergy, 5 mail Gay-Lussac, Neuville sur Oise, 95031 Cergy-Pontoise, France. Tel.: +33 1 34 25 73 60.
E-mail address: christian.david@u-cergy.fr (C. David).

interpreted using a revised Kozeny–Carman equation, showing that fluid flow is strongly affected by the tortuosity of the pore space, which is controlled by the microporosity distribution within the ooids. This study brings new insight into the parameters controlling the physical and mechanical response of oolithic carbonates, and the possible impact on production of geothermal energy at depth or storativity for CO_2 sequestration operations.

1. Introduction

Deformation in porous rocks is a crucial problem in fault development and reservoir management. Active tectonics and extraction of fluids modify the pore pressure in a reservoir, causing variations of the effective stress and possibly leading to faulting and inelastic deformation. The ability to interpret and predict the occurrence and extent of such deformation depends on a fundamental understanding of the mechanical properties (inelastic behavior, failure mode) of porous rocks.

The Oolithe Blanche formation, is one of the two major deep saline aquifers in the Paris Basin (France). This formation has been used for over thirty years in the exploitation of geothermal energy and new wells are still implemented nowadays. This reservoir was also selected by the French geological survey (BRGM) as a potential target for CO_2 geological storage.[1] However, several studies concerning both type of exploitations showed that the Oolithe Blanche forms a complex carbonate reservoir presenting heterogeneous petrophysical and microstructural properties.[2–6]

Many studies using P-wave velocities measurements have shown that dynamic moduli of carbonate rocks are controlled by several microstructural parameters such as rock fabric, pore type and shape, porosity and pore fluid, making it difficult to attribute changes in seismic expression to any one parameter.[3,4,6–15] Elastic waves are, in essence, small mechanical perturbations and are therefore affected by the rock microstructure and rock deformation processes. An effect is thus logically expected on the static moduli, which are directly measured during deformation, and therefore on the overall mechanical response of carbonate rocks. Numerous studies have described mechanical compaction in carbonate rocks.[16–20] The brittle to ductile transition in carbonates shows different attributes than those found in silicate rocks. Limestones undergo the brittle to ductile transition at room temperature for confining pressures accessible in the laboratory[21–24] because calcite requires relatively low shear stresses to initiate mechanical twinning and dislocation. In limestones of intermediate porosity (from 3% to 18%), dilatancy and shear localization is developed under low confining pressure, while strain hardening and shear-enhanced compaction are observed at high confining pressure.[16–18] However at high confining pressure and after a certain amount of strain-hardening, the samples consistently evolve from compaction to dilatancy. This characteristic of dilatant and compactant failure in carbonates is a common feature shared with many types of porous sandstones.[25]

Motivated by the microstructural observations, a number of micromechanical models have been proposed to capture the brittle and ductile failure in porous rock. In the brittle field, models involving pore-emanated crack[26] and sliding wing crack[27–29] have been tested to interpret the experimental data. In relation to these models, analytic estimates of the brittle strength as a function of the initial damage have been derived[20,30,31] and the theoretical predictions can conveniently be compared with laboratory data. In the ductile field, the grain crushing[30,32] and Hertzian fracture[25,33] models have been developed for analyses of pore collapse in carbonate and siliciclastic rocks, respectively. However, considering the extreme heterogeneity of pore systems and microstructures in carbonate rocks, the pore collapse model for limestone[30] would likely be inappropriate in situations where dual porosity is not present, like in carbonates dominated by micritic structures only. To date, there is a lack of microstructural data and observations to constrain more elaborate models.

A key question on the mechanics of inelastic deformation is: how does the starting microstructure of porous carbonates trigger or inhibit the development of inelastic compaction at a given pressure? In this paper, we address this major issue by presenting new physical and mechanical data on porous carbonates with different microstructural settings. We also provide insights on the dominant micromechanism of deformation that leads to macroscopic compaction in porous carbonates. Finally, we investigate the change in ultrasonic velocities and permeability as a function of increasing hydrostatic pressure and deviatoric stress.

2. Sampling and experimental set-up

2.1. Sample selection and preparation

The Oolithe Blanche samples are from the same blocks studied by Casteleyn et al.[3,4] and Makhloufi et al.,[6] who have provided a fully detailed petrophysical description. The blocks come from three quarries located in the Paris Basin (France), in the north of Burgundy near the towns of Massangis (N 47°37′19.22″; E 3°57′22.49″), Bierry-Les-Belles-Fontaines (N 47°36′42.96″; E 4°10′48.78″) and Ravières (N 47°43′34.92″; E 4°14′21.36″) (Fig. 1). The Oolithe Blanche formation is an ooid-rich limestone with minor bioclastic content (echinoderms, bivalves, brachiopods, gastropods, bryozoans and foraminiferas). Ooids found in this limestone show laminations typical of marine ooids formed in a disturbed environment. Macroporosity is not observed and the dominant inter-crystalline microporosity (pore diameter < 10 μm as defined by Lønøy[34]) occurs in a lithified matrix located in the grains and is
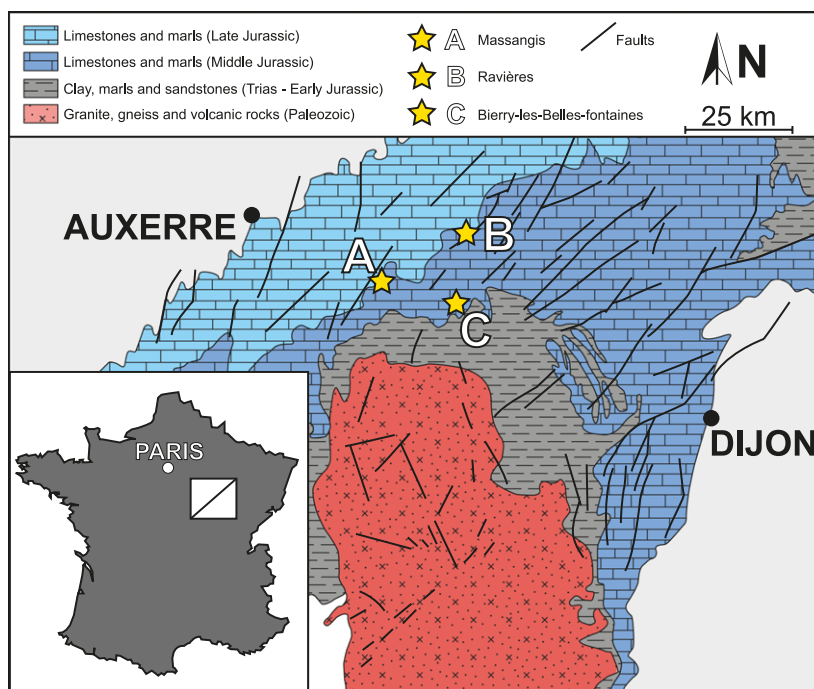
Fig. 1. Geological map of the Eastern part of the Paris Basin, and localization of the three quarries investigated. Simplified from Makhloufi et al.[6]

essentially composed of microcrystalline calcite particles ('micrite', Folk[35]). Two different microstructures are of primary interest here and are linked to the microporosity distribution within the grains: (1) "Uniform porosity" (called hereafter UP) samples with fully microporous grains (Fig. 2(A) and (C)) and (2) "Rimmed porosity" (called hereafter RP) samples displaying microporosity only at the edge of grains (Fig. 2(B) and (D)). Microporous areas are mostly composed of rounded to subrounded particle morphologies, whereas non-microporous parts are essentially made of anhedral morphologies (sensu Deville de Periere et al.[36]) (Fig. 2(E)–(H)).

Two samples of both UP and RP varieties were cored perpendicular to the sedimentary bedding. The size of the cores depended on the analytical protocols to be applied. Porosity and gas permeability at low confining pressure were measured on 25 mm diameter/50 mm length samples, and 40 mm diameter/83 mm length samples were prepared for mechanical deformation and permeability evolution in a triaxial cell.

2.2. Experimental procedure

Porosity of dry samples was measured by the gas expansion method (here nitrogen) at ambient temperature and pressure. Permeability tests were performed with a steady-state nitrogen permeameter (lower limit of 0.001 mD). The nitrogen permeability measurements were made at a confining pressure of 3 MPa and were corrected for the Klinkenberg effect. The mechanical tests were performed in a conventional triaxial cell at the Laboratoire de Géologie of École Normale Supérieure (Paris, France) which is fully described in Ougier-Simonin et al.[37] The hydrostatic and differential stresses were servo-controlled with an accuracy of 0.01 MPa. The confining medium was oil. Pore pressure was driven by a precision volumetric pump. Pore fluid (tap water in equilibrium with $CaCO_3$) was introduced into the sample through the hardened steel platens and we used thin porous steel spacers to distribute the pore fluid on the top and bottom sample surfaces. The pore pressure was kept constant during the experiment. The variation of the pore volume during a test allowed the evolution of volumetric strain to be obtained from the injected or withdrawn volume of water, neglecting the deformation of the solid elements at such low stresses. To perform permeability measurements under stress, a differential pore pressure of 1 MPa was applied between upstream and downstream pressures, inducing a flow through the sample. Accordingly, the permeability can be inferred directly from Darcy's law. Axial strain was measured by three eddy (or Foucault) current sensors mounted externally to the sample[37] with an uncertainty in measurements estimated to 10^{-5}. The samples were jacketed in a perforated neoprene sleeve and a set of 8 piezoceramic transducers is used to measure high frequency P and S-wave velocities along radial directions. Ultrasonic velocities were corrected for radial strain of the samples. Petrographic analyses of average grain size (with a minimum of 500 counts per thin sections) and cement proportion (background analysis technique, expressed in percentage) were conducted on blue dyed thin sections using JmicroVision Image Analysis software (http://www.jmicrovision.com), on both intact rock and post-mortem samples. Thin sections were made along the axial orientation of the samples.

Our objective was not to get a comprehensive knowledge of the mechanical behavior of the selected rocks by building the complete failure envelopes, but to compare
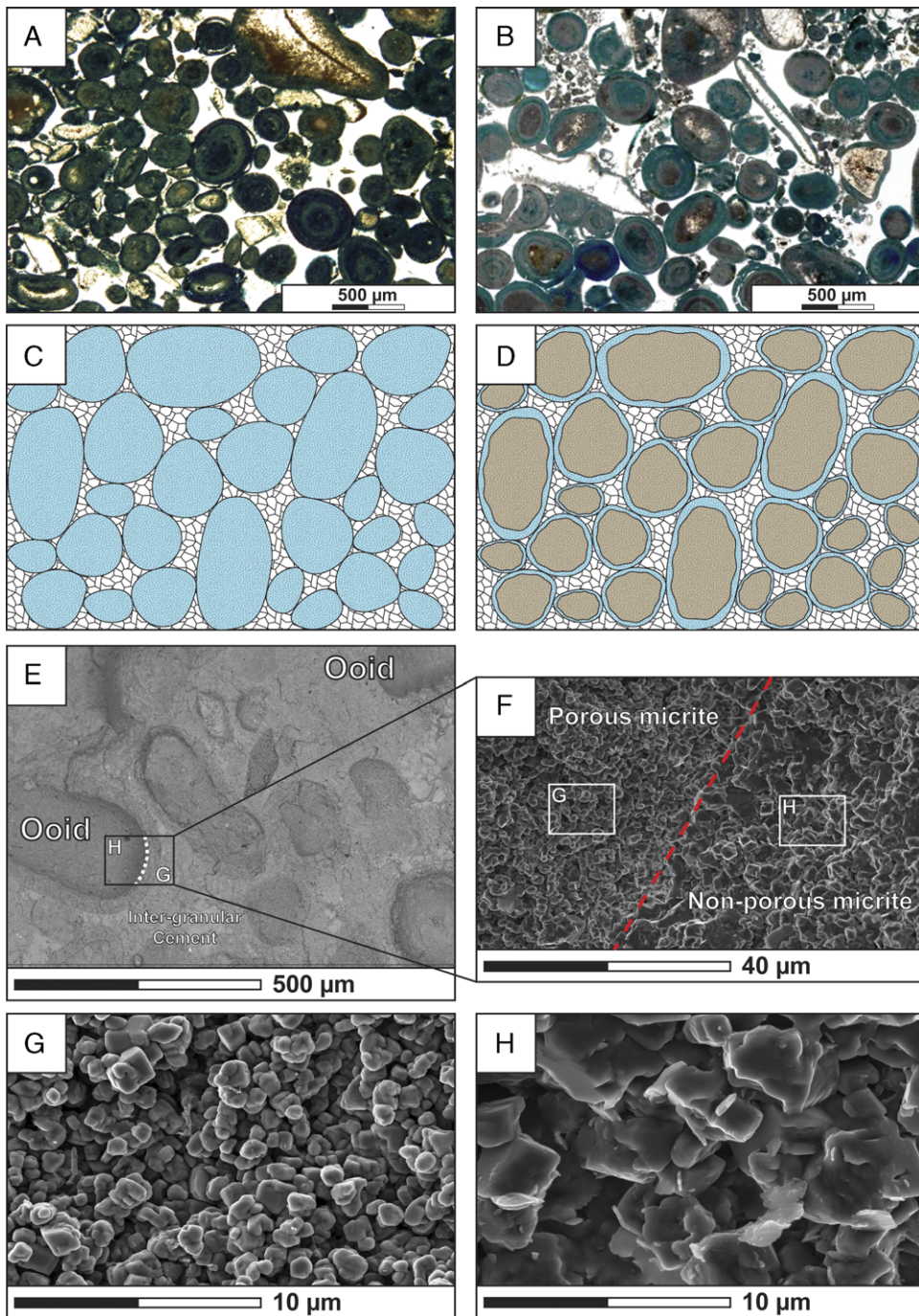
Fig. 2. Pictures of the samples selected for the experiments. The microporosity is dyed in blue color. Ooids can be completely microporous (A) or they can show a rimmed microporosity located on the outside cortex of the ooids (B). C and D: schematic illustration of the two different microstructural attributes. E and F—SEM pictures of a rimmed microporosity ooid, and the boundary between microporous and tight parts (F). The outer part of the cortex (G) display fine grained (1 μm) and the inner part is characterized by tight and coarse anhedral micrites (3 μm). (For interpretation of the references to color in this figure legend, the reader is referred to the web version of this article.)

at a selected stress state how the initial microstructure will affect the hydro-mechanical properties. This was done on two samples taken from each set of UP and RP samples. The stress state that was selected mimics the *in situ* conditions prevailing in the Oolithe Blanche formation in the center of the Paris Basin at a depth of about 2 km. All experiments were carried out under water saturated conditions at an effective confining pressure of 23 MPa (confining pressure P_c = 28 MPa and a pore pressure P_p = 5 MPa) and at a temperature of 55 °C. First, confining and
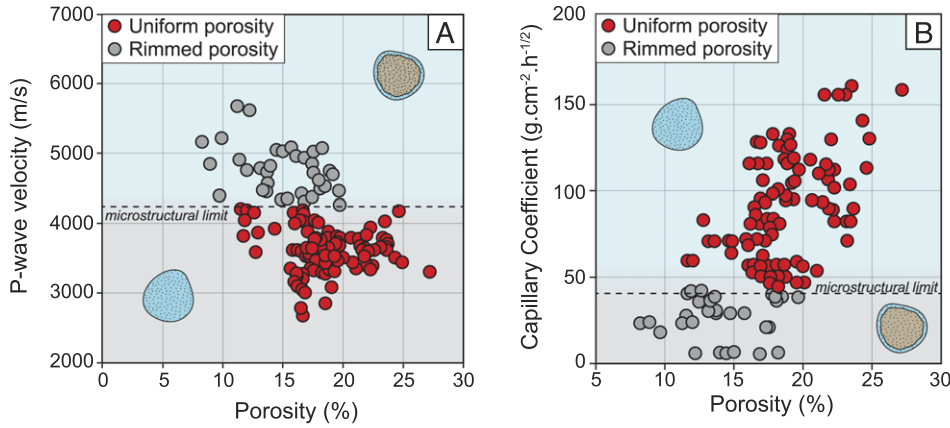
Fig. 3. A—P-wave velocity vs. porosity crossplot. B—Capillary imbibition coefficient vs. porosity cross-plot. The distribution of velocity and capillary coefficient values regarding the microstructural attribute is very clear.
Source: Modified from Casteleyn et al.[3,4] and Makhloufi et al.[6]

Table 1
Petrophysical description of the selected rocks (measured on samples of the same blocks as the selected samples for mechanical testing).

Sample	MA04	RA13	BY11	RA15
Porosity (%)	15.7	15.3	16	15.5
Permeability (mD)	0.06	0.06	0.68	0.13
Pore throat diameter (μm)	0.2	0.23	0.7	0.19
Cement content (%)	4.51	4.55	6.41	6.84
Grain size (μm)	355	440	389	479
Microstructure	Rimmed porosity	Rimmed porosity	Uniform porosity	Uniform porosity

pore pressure were set to 8 and 5 MPa respectively, then temperature was increased to 55 °C. In a second step samples were loaded hydrostatically at the desired confining pressure ($\sigma_1 = \sigma_2 = P_c$), and then the axial stress (σ_1) increased incrementally under controlled axial strain rate (10^{-5} s^{-1}) while maintaining the radial stresses constant. At different stages of deformation, the axial loading ram was locked and the *in situ* permeability was measured as a function of the stress state.

3. Results

In our previous works,[3,4,6] a comprehensive study of the petrophysical properties of the Oolithe Blanche formation has been done on a large set. In particular, variations of elastic wave velocities and transport properties could be linked to specific microstructural attributes. Fig. 3(A) shows that there is a clear separation between the UP samples where the P wave velocity is lower than about 4000 m/s, and the RP samples which have a higher velocity.[4] A similar separation exists for the capillary coefficient derived from spontaneous water imbibition experiments (Fig. 3(B)), with clearly lower values for the RP samples compared to the UP samples.[3] Therefore both microstructural arrangements selected in this study (Fig. 2) are reported to have a specific response for the acoustic and fluid flow properties. We expect similar contrasted results for the mechanical behavior and permeability evolution during deformation between these two microstructural attributes. In order to investigate the microstructural control on the mechanical behavior, the selected samples have similar porosity, grain size, pore

throat diameter (derived from mercury injection tests) and cement content (Table 1). Only the permeability of sample BY11 is different by about one order of magnitude. The Oolithe Blanche formation being a microporous grainstone, the pore network connectivity and thus permeability depends on the distribution of microporosity within the grains (rimmed *vs.* uniform).[6] The difference in the ooids microtexture can be observed on pore-casts (Fig. 4) obtained by dissolving on a surface the calcite matrix using HCl acid after injection of blue-dyed epoxy into the pore space: this technique reveals the three dimensional geometry of the pore space (in blue) for each sample. For the UP sample (Fig. 4(A)), the ooid being fully microporous has a preserved structure on the pore cast, and only the surrounding cement has been removed. In contrast for the RP sample (Fig. 4(B)), the nucleus of the ooid made of nonporous calcite has been completely dissolved, and only the microporous cortex remains.

In the following, we present data from triaxial deformation experiments, with measurement of acoustic properties and permeability evolution under stress.

3.1. Mechanical data

In this paper we use the convention that compressive stresses and compactive strains are positive. The terms σ_1 and σ_3 represent the maximum and the minimum principal stresses. The effective mean stress P' is defined by $P' = \frac{\sigma_1 + 2\sigma_3}{3} - P_p$ and the deviatoric stress Q is defined by $Q = \sigma_1 - \sigma_3$. Two different types of mechanical behaviors were observed regarding the microstructural parameter:
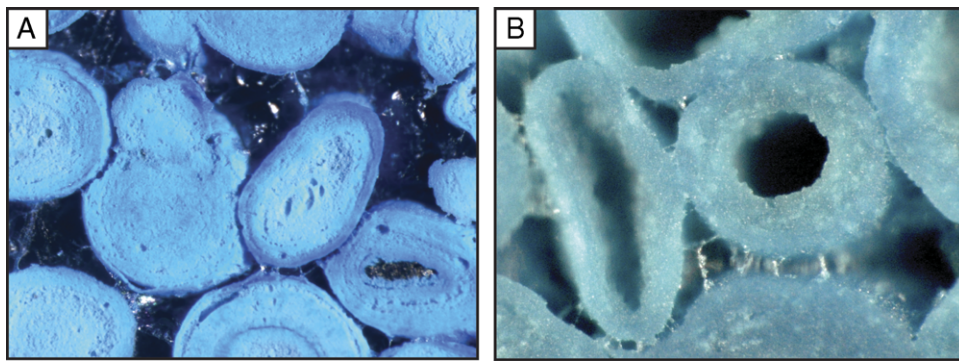
Fig. 4. Pore casts obtained on Oolithe Blanche samples in which blue-dyed epoxy has been injected into the pore space. A—Uniform porosity sample with fully microporous grains. B—Rimmed porosity sample where the non-porous inner cortex has been dissolved by HCl. (For interpretation of the references to color in this figure legend, the reader is referred to the web version of this article.)
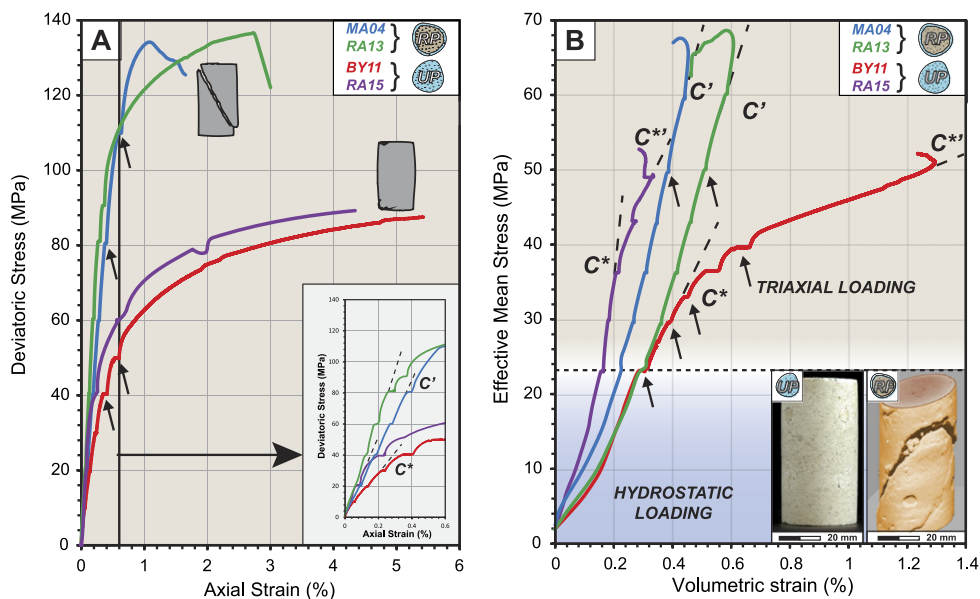*Source:* From Makhloufi.[5]

Fig. 5. A—Deviatoric stress vs. axial strain plot. The zoomed part corresponds to the first 0.6% of axial deformation. B—Effective mean stress vs. volumetric strain plot, during hydrostatic and triaxial loading. Black arrows indicate creep stages induced by the axial ram locking during permeability measurements. Uniform porosity samples have a slight barrel shape typical of ductile behavior, whereas Rimmed porosity samples present shear fractures (imaged using X-ray scanning) typical of brittle behavior. (For interpretation of the references to color in this figure legend, the reader is referred to the web version of this article.)

(1) UP samples with fully microporous grains (BY11 and RA15, red and purple curves respectively in Fig. 5) have a typical behavior of the compactive cataclastic flow regime, where both samples display similar differential stress-axial strain curves (Fig. 5(A)). Indeed, both samples exhibit strain hardening, large strains and no stress drop. On the effective mean stress vs. volumetric strain plot (Fig. 5(B)), the triaxial curves coincide with the hydrostat up to the onset of shear-enhanced compaction at critical stress C^*.[25] Beyond these stress levels, the deviatoric stress provided a significant contribution to the compactive strain, and shear-enhanced compaction is observed. Creep deformation appeared when the axial loading ram was locked during permeability measurements (arrows). Porosity reduction went up to 1.3% for BY11 and 0.35% for RA15 before

reaching the critical stress state $C^{*\prime}$ corresponding to the progressive evolution from shear-enhanced compaction to shear-induced dilation, as the amount of cracks created in the samples progressively rose during deformation. No shear localization was observed in the samples after the experiments but a slight barrel shape (Fig. 5(A)) for both samples with scarce induced fractures perpendicular to σ_1 probably due to unloading. All those features are common attributes of the cataclastic flow (or ductile) regime.

(2) Samples showing a rimmed porosity within the grains (MA04 and RA13, the blue and green curves respectively) are characterized by a very linear elastic deformation. A clear deviatoric stress drop was observed around 135 MPa associated with an axial deformation of 1.2% and 2.7% for MA04 and RA13, respectively
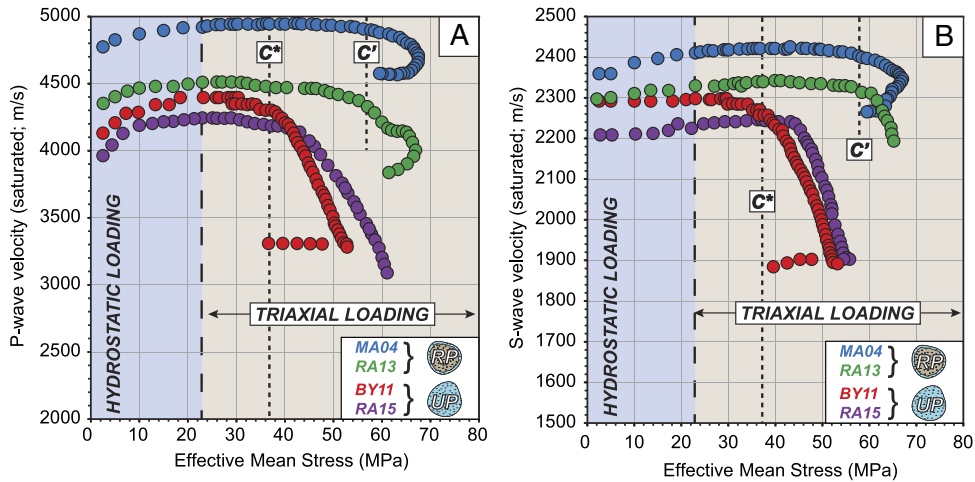
Fig. 6. P and S-wave velocity evolution during hydrostatic and triaxial loading. C^* corresponds to the onset of shear-enhanced compaction, and C' corresponds to the onset of shear-induced dilation.

(Fig. 5(A)). After that peak stress, strain softening was observed and the stress dropped to a residual level. A deviation from the hydrostatic loading (dashed curve) was observed and implies a modification in the change of porosity, induced by the deviatoric stress Q.[15] The C' point represents the onset of shear-induced dilation, beyond which the applied stress forces the pore space to dilate. The compaction decelerates in comparison to the hydrostat with a reduction of the volumetric strain as the effective mean stress increases (Fig. 5(B)). The volumetric strain for rimmed porosity samples does not exceed 0.6%. A very weak creep deformation was observed when the axial stress was maintained stable during permeability measurements. The end of the experiment is marked by a localization of the deformation on a shear fracture oriented at an intermediate angle (40°–45°) with respect to the principal stress (Fig. 5(A)). All those features are common attributes of the brittle fracture regime.

3.2. Acoustic properties

The effects of hydrostatic loading and differential stress on both radial P and S-wave velocities were analyzed during the four experiments. Fig. 6 summarizes the velocity measurements for each sample. We plot the elastic wave velocities as a function of effective mean stress. It is noteworthy that the overall trend of acoustic wave evolution during the experiment was similar for samples displaying the same microstructure. During hydrostatic loading both P and S wave velocities increased (Fig. 6), probably due to the closure of pre-existing microcracks. After the hydrostatic loading stage, two types of velocity evolution were observed depending on the microstructural texture:

(1) For UP samples, the P and S-wave velocities reached a plateau during the first stage of triaxial loading from 23 to ~32 MPa effective mean stress. For V_p(BY11), V_p(RA15) and V_s(BY11) a good agreement

was found between the onset of inelastic compaction at C^* and the decrease in P and/or S wave velocities, whereas a small offset was observed for V_s(RA15). The large velocity decrease is linked to the larger strain experienced by these samples.

(2) RP samples are characterized by an increase of P and S-wave velocities at the beginning of axial loading, until ~40 MPa of effective mean stress. Then, they reached a plateau just before showing a gentle drop while reaching the stress state C'. Beyond this onset of shear-induced dilation, a large decrease of both P and S-wave velocities was observed.

3.3. Permeability evolution

The permeability evolution as a function of effective mean stress is shown in Fig. 7. Permeability slowly decreases during hydrostatic loading for both uniform and rimmed porosity samples. Under triaxial loading, contrasted permeability evolution appears:

(1) UP samples are characterized by a diminution of permeability during the first stage of triaxial loading, until the stress state C^*. This critical stress state marks the onset of an acceleration of permeability reduction. When approaching the critical stress state $C^{*'}$ and beyond, corresponding to the onset of shear-induced dilation, the permeability of RA15 sample rises from 0.18 to 0.37 mD.

(2) RP samples are characterized by a slight diminution of permeability during the first stage of triaxial loading. While the effective mean stress rises (from 35 to 50 MPa), sample MA04 shows a rather flat trend where permeability is stable before a slight augmentation near the stress state C', marking the beginning of shear-induced dilation. Sample RA13 is characterized by a sharper drop of permeability values between 35 and 50 MPa of effective mean stress, before a smooth increase near the onset of shear-induced dilation.
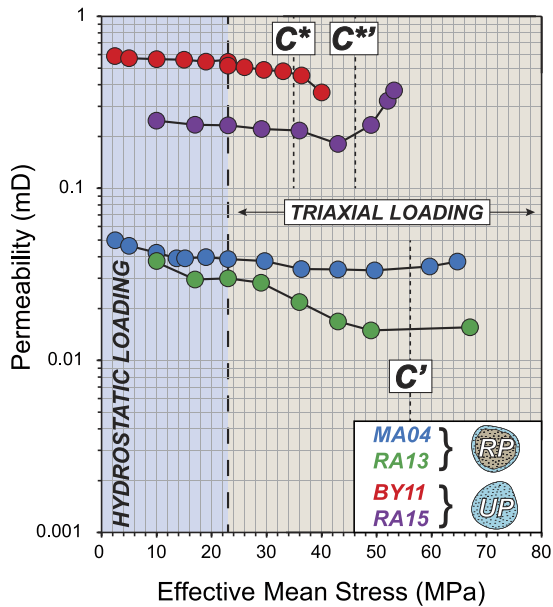
Fig. 7. Permeability evolution during hydrostatic and triaxial loading. C^* corresponds to the onset of shear-enhanced compaction, and C' corresponds to the onset of shear-induced dilation.

3.4. Microstructural observations

Samples were unloaded and retrieved from the pressure vessel at the end of the experiments. The deformed samples were first impregnated with epoxy and then sawed along a plane parallel to the axial direction to prepare petrographic thin sections. To characterize deformation features in the microporous ooids, Scanning Electron Microscope (SEM) is used. Fig. 8 presents a selection of pictures for two samples with contrasted microstructure and mechanical behavior.

(1) In the UP samples at microstructural scale, few cracks appear in the calcite cements coupled with an intense twinning activity (Fig. 8(D), (F) and (H)). This twinning does appear as an important deformation mechanism in this sample.
(2) Microstructural deformation features consist of cracks and twinning localized in calcite cements. Cracks appear mainly near macroscopic shear zones whereas twinning activity is widespread in the sample (Fig. 8(C), (E) and (G)).

4. Discussion

4.1. Influence of microporosity distribution on the elastic properties

In our previous studies on the Oolithe Blanche formation,[3,4] P-wave velocities measurements have shown that the dynamic moduli are controlled by the microporosity distribution within the ooids, suggesting that UP samples are characterized by a higher compliance than RP samples. The same observation can be made on the P and S-wave velocity evolution through deformation in the

present work (Fig. 6): UP samples clearly display lower velocities than RP samples. A similar conclusion can also be drawn on the static moduli (Fig. 5(A)) where the RP samples are stiffer (although it is not that obvious for RA15) than the UP samples. This result is of primary importance for the Oolithe Blanche formation, and in general for carbonate rock reservoirs, when dealing with reservoir depletion phenomenon during production. The difference in elastic properties can be easily explained by the contrasted values of the bulk modulus between the ooids whether they are composed of porous micrites (K_P) or tight micrites (K_T), with $K_T > K_P$ (Fig. 9). Consequently, the bulk modulus K_{RP} of the ooids in the RP samples can be considered as the effective moduli K_{EFF} of both the porous micrite (K_P) and the tight micrite (K_T) which can be calculated for example using the Hashin–Shtrikman scheme;[38] this leads to $K_{EFF} > K_P$. As the calcite cement located between the ooids with compressibility K_C is assumed to have the same influence on the elastic properties for both the RP and UP samples, it is expected that the RP samples are characterized by a lower compressibility than the UP samples (Fig. 9(A) and (B)). Recent studies of microhardness estimation on similar rocks (oolithic grainstone with rimmed microporosity,[39]), and P-wave velocity data on porous and tight micrites[40] tend to confirm this hypothesis. However a contrast in compressibility cannot explain the observed difference in mechanical behavior (brittle or ductile) of the samples regarding the microstructural attribute.

4.2. Influence of microporosity distribution on the mechanical behavior

Mechanical properties of porous rocks can be analyzed from two complementary points of view. One approach is to assume a continuous medium in which pores (and cracks) can be considered as inclusions. This approach has been successfully developed many years ago for elastic properties[41,42] and provides in general more relevant results when the porosity is low. At the other extreme, another approach is to consider a porous rock as a granular medium.[43] The granular models are more appropriate for high porosity rocks. They have been improved by bonding grains[44] or considering identical spherical grains and focusing on the contact of two spheres[45] as a key feature.

Real porous rocks, however, fall between these two extreme viewpoints, because they are made of grains that are cemented. Our samples are characterized by a very low cement proportion (5%), which is quite unusual for cemented grainstones.[46] Consequently, we suggest and consider that our samples can be seen as a grain-supported or granular medium, where ooids constitute the skeleton of the rock. This assumption is somehow confirmed by the deformation micromechanisms observed in deformed samples (Fig. 8), where calcite twinning and microcracks are observed in both samples, regardless of the microporosity distribution. The only difference observed is that calcite twining seems to be much more intense in UP samples, which can be explained by the higher amount of axial strain they underwent during the experiments.
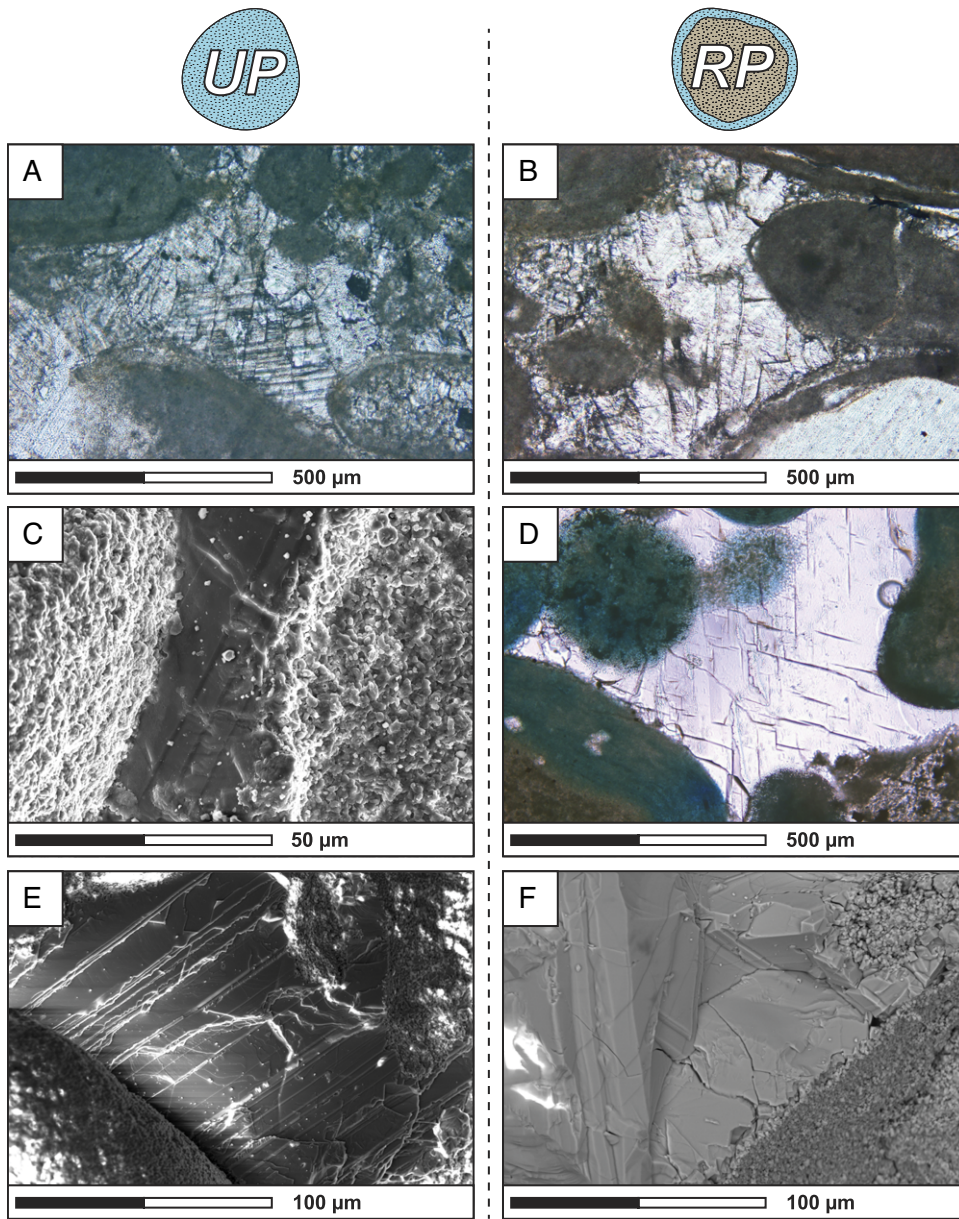
Fig. 8. Micrographs of samples after mechanical testing. A, C and E display calcite twining in the cemented parts, in optical microscopy and SEM imaging (RA15 and RA13 samples). B, D and F display microcracks located in the calcite cements in optical microscopy and SEM imaging. These microcracks do not propagate in the ooids.

Therefore, grain contacts become a key feature to understand the observed mechanical behavior. As our goal is to understand how the contrast in microporosity distribution leads to different mechanical behaviors, we need to compare our observations to a conceptual model for rock failure. For sake of simplicity we decided to use the 2D granular model proposed by Guéguen and Fortin[47] in a qualitative way. In this model the authors make the assumption that grain to grain contacts are key features controlling the mechanical response of uncemented granular rocks, and propose an elastic envelope with two straight lines on a P–Q plot, delimited by the value T_0, which represents the local tensile stress between grains, and the value

of P^*. Both lines intersect at the transition between brittle and ductile domains.[47] In oolithic carbonate rocks, we have to consider here the role of the micrite grains. Both UP and RP samples display fine micrite particles (1–3 μm), but their morphologies are significantly different (Fig. 9(C) and (D)). UP samples are composed of rounded micrites characterized by punctic to partially coalescent contacts, whereas RP samples are made of anhedral micrites characterized by fully coalescent contacts between particles. When extrapolating the mechanical behavior of those two morphologies in the case of a deformation, (1) rounded micrites in UP samples have a structure similar to that of an ill-cemented granular material prone to experience
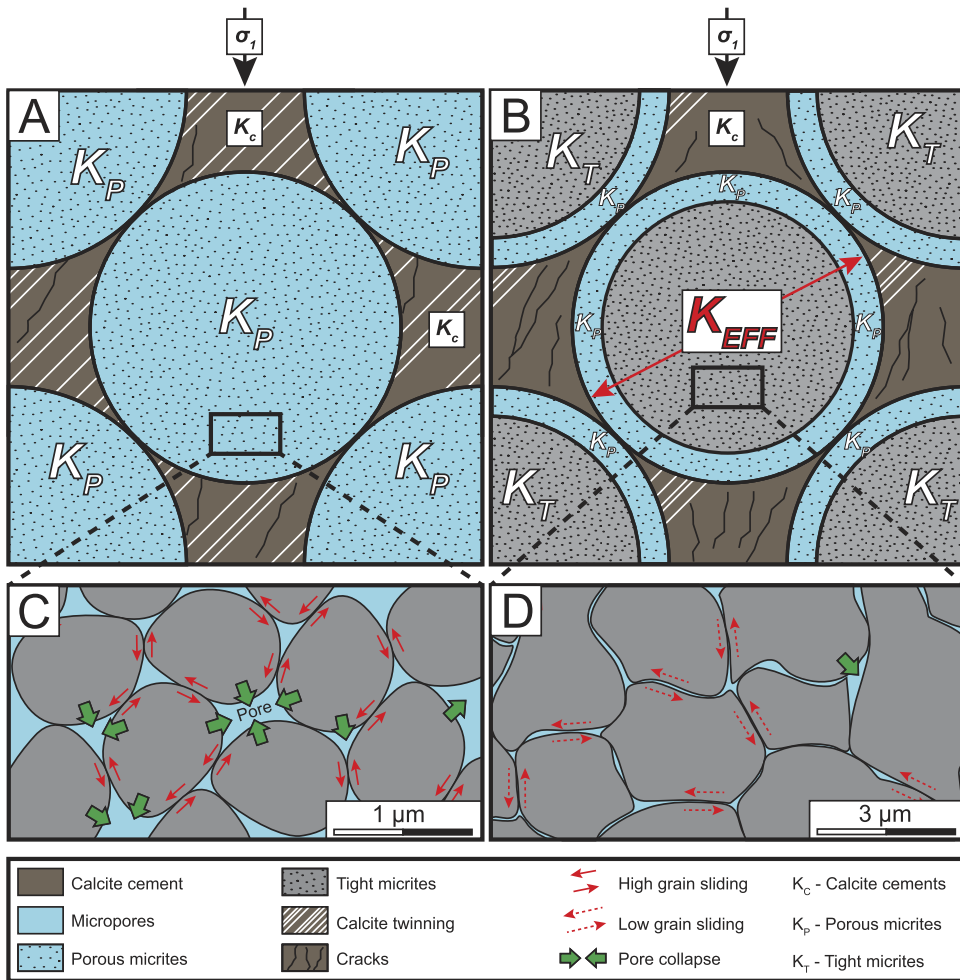
Fig. 9. Schematic view of the samples regarding the microstructural attribute (A—uniform porosity or B—Rimmed porosity), deformation features (twining, cracking, sliding, collapse), micrite description (C—rounded, D—Anhedral) within the ooids.

significant compaction and pore collapse (Fig. 9(C)), and (2) anhedral micrite in RP samples form a tight arrangement prone to sliding at grain contacts with little compaction (Fig. 9(D)). This could lead to a higher value of pore collapse pressure P^* in RP samples than in UP samples, while the tensile strength T_o in the model,[47] mostly related to the cement properties, would remain the same. Then, considering this contrast in P^*, the 2D granular model[47] predicts that if we follow the same stress path (Fig. 10), we will reach the brittle envelope for RP samples, and the ductile envelope for UP samples, in agreement with our observations. This is so because the critical pressure P^* is a controlling parameter for the shape and extension of the failure envelope in porous rocks.[25]

4.3. Influence of microporosity distribution on the permeability

Rimmed porosity samples display lower permeability values compared to uniform porosity samples, although they both have a similar total porosity. This observation is consistent with our previous studies focusing on
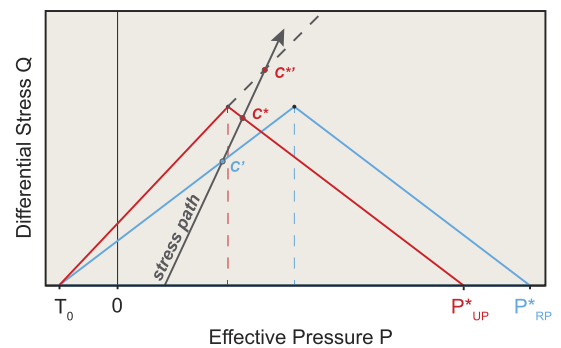

Fig. 10. Conceptual failure envelope model based on the expected variability of the critical pressure P^* with microporosity texture. The triaxial loading path intersects the ductile envelope for UP samples and the brittle one for RP samples.

the capillary coefficient values of the Oolithe Blanche formation, which is often used as a proxy for transport properties[3,4,6] (Fig. 3). This effect is clearly the reflection of two different microstructural attributes of the porous media, and can be related to the contrast in tortuosity

when comparing UP and RP samples.[6] To estimate the tortuosity contrast for flow through our granular media, we use here a revised Kozeny–Carman equation proposed by Walsh and Brace[48] and Costa,[49] where the permeability k is calculated from:

$$k = \frac{\phi m^2}{b\tau^2}$$

where ϕ is the porosity, b is equal to 2 for flow through pipe-like pores, m is the hydraulic radius, and τ is the tortuosity. The measured porosity, cement proportion and mean grain size are similar[6] for UP and RP samples (Table 1). Concerning the hydraulic radii, we can assume that the values should also be very close, looking at the small variability of the mean throat diameter except for sample BY11 which has a higher mean pore throat diameter and consistently a higher permeability (Table 1). The pore throat diameter derived from mercury injection tests is another microstructural characteristic of the pore space which is often used in models for permeability predictions. Consequently the grain network architecture in terms of grain contact types and coordination number between ooids are similar, and therefore the permeability is primarily related to the tortuosity contrast. In the case of RP samples, the fluid path within the ooids is characterized by a high tortuosity since the fluid needs to bypass/get around the non-porous inner cortex of the ooids (Fig. 4). A lower bound for the actual travel path length in a RP ooid can be estimated by half the perimeter πR of the ooid (assumed to have a spherical shape), where R is the radius of the ooid. On the other hand, in UP samples, the fluid can directly get through the porous grain, crossing the UP ooid over a distance $2R$. The pore-casts in Fig. 4 highlight the increased path length for a fluid molecule to cross the porous medium in RT samples compared to UP samples. The predicted lower bound permeability ratio between RP and UP samples is then:

$$\frac{k_{UP}}{k_{RP}} = \left(\frac{\pi R}{2R}\right)^2 = \left(\frac{\pi}{2}\right)^2.$$

This ratio equal to 2.46 is in agreement with the lower bound of the measured permeability ratio between the UP and RP samples derived from Table 1, which is approximately 2. With similar microstructural parameters (porosity, grain size, coordination number), UP and RP samples have different permeability values which are explained by the variation of tortuosity.

4.4. Shear-induced dilation: an effective mechanism for permeability enhancement

A key conclusion we draw here is that there is a good correspondence between permeability changes and shear-induced dilation (Fig. 7). This phenomenon was already observed in porous sandstones[50] and some carbonates,[51] but being able to observe permeability rise through dilation during a triaxial experiment is not that simple. The onset of shear-induced dilation, C' for RP samples and $C^{*\prime}$ for UP samples, map out a boundary between two domains regarding the permeability evolution. Here, the inelastic deformation induced by dilation processes is related to the

opening of microcracks and the corresponding increase of crack density, especially at the grain/cement interfaces. This is also in agreement with the P and S-wave velocity evolution as they decrease during the shear-induced dilation, which can only be explained by the nucleation and propagation of microcracks.[52] Both factors (opening of microcracks and increase of crack density) would enhance the local hydraulic conductances around the ooids resulting in an overall increase of permeability. Interestingly, this process is even more effective for UP samples (RA15) that first underwent shear-enhanced compaction but without a significant change in porosity (volumetric strain $\sim$ 0.4%). The microcracks become permeability efficient once the sample reached the onset of shear-induced dilation accompanied by pore volume increase. This shows that deformation and fluid transport are coupled in a complex manner. The quantitative modeling of the permeability enhancement is beyond the scope of this paper, but this is a major issue that need to be investigated in the future.

5. Conclusion

The microporosity distribution is a key feature controlling the physical properties and mechanical behavior of oolithic carbonate rocks from the Eastern Paris Basin. Two different micrite microtextures were investigated, all other parameters being constant: (i) uniform porosity (UP) samples with microporosity uniformly distributed in the ooids and (ii) rimmed porosity (RP) samples where the microporosity is present only on the edge of the ooids. Mechanical tests at a selected stress state aimed at mimicking the in situ stress and temperature condition at two kilometers depth in the central Paris basin were conducted on both types of samples, showing different behaviors which can be summarized as follows:

(1) The elastic wave velocities in uniform porosity (UP) samples are lower than in rimmed porosity (RP) samples, showing a larger compliance in the former directly linked to the uniform distribution of microporosity,

(2) The mechanical behavior for UP sample is "ductile" (compactive cataclastic flow) and brittle for RP samples, which can be interpreted by a simple failure envelope model where the critical pressure P^* for RP samples is significantly higher than for UP samples,

(3) The permeability of UP samples is higher than that of RP samples, which can be interpreted by a significant higher tortuosity in the latter.

This study shows that porous carbonate rocks can display a complex behavior regarding their microstructural attribute, which can strongly influence both the mechanical stability at depth and the transport properties, two key parameters for a reservoir rock considered as a potential target for CO_2 storage or geothermal energy recovery. In addition, the work presented here will greatly benefit the prediction and assessment of porous and permeable bodies within a complex carbonate reservoir such as the Oolithe Blanche formation.

Acknowledgments

References

[1] Brosse E, Badinier G, Blanchard F, Caspard E, Collin PY, Delmas J, Dezayes C, Dreux R, Dufournet A, Durst P, Fillacier S, Garcia D, Grataloup S, Hanot F, Hasanov V, Houel P, Kervevan C, Lansiart M, Lescanne M, Menjoz A, Monnet M, Mougin P, Nedelec B, Poutrel A, Rachez X, Renoux P, Rigollet C, Ruffier-Meray V, Saysset S, Thinon I, Thoraval A, Vidal-Gilbert S. Selection and characterization of geological sites able to host a pilot-scale CO_2 storage in the Paris basin (GeoCarbone-PICOREF). *Oil Gas Sci Technol*. 2010;65: 375e403.

[2] Delmas J, Brosse E, Houel P. Petrophysical properties of the Middle Jurassic carbonates in the PICOREF Sector (South Champagne, Paris Basin, France). *Oil Gas Sci Technol Rev Inst Fr Pét*. 2010;65: 405–434.

[3] Casteleyn L, Robion P, Collin P-Y, Menéndez B, David C, Desaubliaux G, Fernandes N, Dreux R, Badiner G, Brosse E, et al. Interrelations of the petrophysical, sedimentological and microstructural properties of the Oolithe Blanche Formation (Bathonian, saline aquifer of the Paris Basin). *Sediment Geol*. 2010;230:123–138.

[4] Casteleyn L, Robion P, David C, Collin P-Y, Menéndez B, Fernandes N, Desaubliaux G, Rigollet C. An integrated study of the petrophysical properties of carbonate rocks from the "Oolithe Blanche" formation in the Paris Basin. *Tectonophysics*. 2011;503:18–33.

[5] Makhloufi Y. *Impact de la sédimentologie et de la diagenèse sur les propriétés pétrophysiques d'un réservoir carbonaté oolithique. Le cas de la Formation de l'Oolithe Blanche (Bathonien, Bassin de Paris, France)* [Ph.D. thesis]. Paris 6: Université Pierre et Marie Curie; 2013:196 pages.

[6] Makhloufi Y, Collin P-Y, Bergerat F, Casteleyn L, Claes S, David C, Menéndez B, Monna F, Robion P, Sizun J-P, et al. Impact of sedimentology and diagenesis on the petrophysical properties of a tight oolitic carbonate reservoir. The case of the Oolithe Blanche Formation (Bathonian, Paris Basin, France). *Mar Pet Geol*. 2013;48: 323–340.

[7] Anselmetti FS, Eberli GP. Controls on sonic velocity in carbonates. *Pageoph*. 1993;141:287–323.

[8] Anselmetti FS, Eberli GP. The velocity-deviation log: A tool to predict pore type and permeability trends in carbonate drill holes from sonic and porosity or density logs. *AAPG Bull*. 1999;83:450–466.

[9] Kenter J, Podladchikov F, Reinders M, Van der Gaast S, Fouke B, Sonnenfeld M. Parameters controlling sonic velocities in a mixed carbonate-siliciclastics Permian shelf-margin (upper San Andres formation, Last Chance Canyon, New Mexico). *Geophysics*. 1997;62: 505–520.

[10] Kenter JaM, Anselmetti FS, Kramer PH, Westphal H, Vandamme MGM. Acoustic properties of "young" carbonate rocks, ODP Leg 166 and boreholes Clino and Unda, Western Great Bahama Bank. *J Sediment Res*. 2002;72:129–137.

[11] Kenter J, Braaksma H, Verwer K, van Lanen X. Acoustic behavior of sedimentary rocks: Geologic properties versus Poisson's ratios. *Leading Edge*. 2007;26:436–444.

[12] Assefa S, McCann C, Sothcott J. Velocities of compressional and shear waves in limestones. *Geophys Prospect*. 2003;51:1–13.

[13] Verwer K, Braaksma H, Kenter J. Acoustic properties of carbonates: Effects of rock texture and implications for fluid substitution. *Geophysics*. 2008;73:B51–B65.

[14] Weger RJ, Eberli GP, Baechle GT, Massaferro JL, Sun Y-F. Quantification of pore structure and its effect on sonic velocity and permeability in carbonates. *AAPG Bull*. 2009;93:1297–1317.

[15] Brigaud B, Vincent B, Durlet C, Deconinck J-F, Blanc P, Trouiller A. Acoustic properties of ancient shallow-marine carbonates: effects of depositional environments and diagenetic processes (Middle Jurassic, Paris Basin, France). *J Sediment Res*. 2010;80: 791–824.

[16] Baud P, Schubnel A, Wong T-F. Dilatancy, compaction and failure mode in Solnhofen limestone. *J Geophys Res*. 2000;195: 19289–19303.

[17] P Baud, David,C Vinciguerra, A Cavallo, E Walker, T Reuschle, Compaction and failure in high porosity carbonates: Mechanical data and microstructural observations, 2009.

[18] Vajdova V, Baud P, Wong T-F. Compaction, dilatancy and failure in porous carbonate rocks. *J Geophys Res*. 2004;109:B05204 http://dx.doi.org/10.1029/2003JB002508.

[19] Vajdova V, Zhu W, Chen T-MN, Wong T-F. Micromechanics of brittle faulting and cataclastic flow in Tavel limestone. *J Struct Geol*. 2010; 32:1158–1169.

[20] Wong TF, Baud P. The brittle-ductile transition in porous rock: A review. *J Struct Geol*. 2012;44(2012):25–53.

[21] Robertson EC. Experimental study of the strength of rocks. *Bull Geol Soc Am*. 1955;66:1275–1314.

[22] Paterson MS. Experimental deformation and faulting in Wombeyan marble. *Geol Soc Am Bull*. 1958;69(4):465–476.

[23] Heard HC. Transition from brittle fracture to ductile flow in Solnhofen limestone as a function of temperature, confining pressure and interstitial fluid pressure. In: Griggs D, Handin J, eds. *Rock Deformation*. 1960:193–226, Memoir. Geological Society of America, vol. 79.

[24] Evans B, Fredrich J, Wong T-F. The brittleeductile transition in rocks: recent experimental and theoretical progress. In: Duba AG, Durham WB, Handin JW, Wang HF, eds. *The Heard Volume*. Am. Geophys. Union Geophysical Monograph, vol. 56. 1990:1–20.

[25] Wong T-F, David C, Zhu W. The transition from brittle faulting to cataclastic flow in porous sandstones: mechanical deformation. *J Geophys Res*. 1997;102:3009–3025.

[26] Sammis CG, Ashby MF. The failure of brittle porous solids under compressive stress states. *Acta Metall*. 1986;34:511–526.

[27] Horii H, Nemat-Nasser S. Brittle failure in compression: splitting, faulting and brittle-ductile transition. *Philos Trans R Soc Lond*. 1986; 319:337–374.

[28] Ashby MF, Sammis CG. The damage mechanics of brittle solids in compression. *Pure Appl Geophys*. 1990;133:489–521.

[29] Kemeny JM, Cook NGW. Micromechanics of deformation in rocks. In: Shah SP, ed. *Toughening Mechanisms in Quasi-Brittle Materials*. Klewer Academic; 1991:155–188.

[30] Zhu W, Baud P, Wong TF. Micromechanics of cataclastic pore collapse in limestone. *J Geophys Res Solid Earth (1978–2012)*. 2010; 115(B4).

[31] Zhu W, Baud P, Vinciguerra S, Wong T-F. Micromechanics of brittle faulting and cataclastic flow in Alban Hills tuff. *J Geophys Res*. 2011; 116:B06209.

[32] Curran JH, Carroll MM. Shear stress enhancement of void compaction. *J Geophys Res*. 1979;84:1105–1112.

[33] Zhang J, Wong T-F, Davis DM. Micromechanics of pressure-induced grain crushing in porous rocks. *J Geophys Res*. 1990;95:34–352.

[34] Lønøy A. Making sense of carbonate pore systems. *AAPG Bull*. 2006; 90:1381–1405.

[35] Folk RL. A review of grain-size parameters. *Sedimentology*. 1966;6: 73–93.

[36] Deville de Periere M, Durlet C, Vennin E, Lambert L, Bourillot R, Caline B, Poli E. Morphometry of micrite particles in cretaceous microporous limestones of the Middle East: Influence on reservoir properties. *Mar Pet Geol*. 2011;28:1727–1750.

[37] Ougier-Simonin A, Fortin J, Guéguen Y, Schubnel A, Bouyer F. Cracks in glass under triaxial conditions. *Internat J Engrg Sci*. 2011;49(1): 105–121.

[38] Hashin Z, Shtrikman S. A variationnal approach to the elastic behavior of multiphase materials. *J Mech Phys Solids*. 1963;11: 127–140.

[39] Ghabezloo S, Sulem J, Guédon S, Martineau F. Effective stress law for the permeability of a limestone. *Int J Rock Mech Min Sci*. 2008; http://dx.doi.org/10.1016/j.ijrmms.2008.05.006.

[40] Regnet JB, Robion P, David C, Fortin J, Brigaud B, Yven B. Acoustic and reservoir properties of microporous carbonate rocks: implication of micrite particle size and morphology. *J Geophys Res Solid Earth*. 2015.

[41] Mackenzie JK. The elastic constants of a solid containing spherical holes. *J Geophys Res*. 1950;B63(2):2–11.

[42] Eshelby JD. The determination of the elastic field of an ellipsoidal inclusion, and related problems. *Proc R Soc Lond Ser A*. 1957;241: 376–396.

[43] Brandt H. A study of the speed of sound in porous granular media. *J Appl Mech*. 1955;22:479–486.

[44] Digby PJ. The effective elastic moduli of porous granular rocks. *J Appl Mech*. 1981;48:803–808.

[45] Walton K. The effective elastic moduli of a random packing of spheres. *J Mech Phys Solids*. 1960;35(2):213–226.

[46] Scholle PA, Ulmer-Scholle DS. *A Color Guide to the Petrography of Carbonate Rocks: Grains, Textures, Porosity, Diagenesis*. AAPG Memoir, vol. 77. AAPG; 2003.

[47] Guéguen Y, Fortin J. Elastic envelopes of porous sandstones. *Geophys Res Lett*. 2013;40:3550–3555. http://dx.doi.org/10.1002/grl.50676. 2013.

[48] Walsh JB, Brace WF. The effect of pressure on porosity and the transport properties of rock. *J Geophys Res*. 1984;89:9425–9431.

[49] Costa A. Permeability–porosity relationship: A reexamination of the Kozeny-Carman equation based on a fractal pore-space geometry assumption. *Geophys Res Lett*. 2006;33:L02318 http://dx.doi.org/10.1029/2005GL025134.

[50] David C, Menendez B, Zhu W, Wong TF. Mechanical compaction, microstructures and permeability evolution in sandstones. *Phys Chem Earth, Part A: Solid Earth Geodesy*. 2001;26(1):45–51.

[51] Zhu W, Wong TF. The transition from brittle faulting to cataclastic flow: Permeability evolution. *J Geophys Res Solid Earth (1978–2012)*. 1997;102(B2):3027–3041.

[52] J Fortin, Y Guéguen, A Schubnel, Effects of pore collapse and grain crushing on ultrasonic velocities and Vp/Vs, 2007.